

NRC Publications Archive Archives des publications du CNRC

A large molecular gas reservoir in the protocluster SPT2349–56 at $z = 4.3$

Zhou, Dazhi; Chapman, Scott C.; Sulzenauer, Nikolaus; Hill, Ryley; Aravena, Manuel; Araya-Araya, Pablo; Cathey, Jared; Marrone, Daniel P.; Phadke, Kedar A.; Reuter, Cassie; Solimano, Manuel; Spilker, Justin S.; Vieira, Joaquin D.; Vizgan, David; Wang, George C. P.; Weiss, Axel

This publication could be one of several versions: author's original, accepted manuscript or the publisher's version. / La version de cette publication peut être l'une des suivantes : la version prépublication de l'auteur, la version acceptée du manuscrit ou la version de l'éditeur.

For the publisher's version, please access the DOI link below. / Pour consulter la version de l'éditeur, utilisez le lien DOI ci-dessous.

Publisher's version / Version de l'éditeur:

<https://doi.org/10.3847/2041-8213/adb8d8>

The Astrophysical Journal Letters, 982, 1, 2025-03-17

NRC Publications Archive Record / Notice des Archives des publications du CNRC :

<https://nrc-publications.canada.ca/eng/view/object/?id=fcaaf73c-3a54-4765-b258-1caa7dc3c0b4>

<https://publications-cnrc.canada.ca/fra/voir/objet/?id=fcaaf73c-3a54-4765-b258-1caa7dc3c0b4>

Access and use of this website and the material on it are subject to the Terms and Conditions set forth at

<https://nrc-publications.canada.ca/eng/copyright>

READ THESE TERMS AND CONDITIONS CAREFULLY BEFORE USING THIS WEBSITE.

L'accès à ce site Web et l'utilisation de son contenu sont assujettis aux conditions présentées dans le site

<https://publications-cnrc.canada.ca/fra/droits>

LISEZ CES CONDITIONS ATTENTIVEMENT AVANT D'UTILISER CE SITE WEB.

Questions? Contact the NRC Publications Archive team at

PublicationsArchive-ArchivesPublications@nrc-cnrc.gc.ca. If you wish to email the authors directly, please see the first page of the publication for their contact information.

Vous avez des questions? Nous pouvons vous aider. Pour communiquer directement avec un auteur, consultez la première page de la revue dans laquelle son article a été publié afin de trouver ses coordonnées. Si vous n'arrivez pas à les repérer, communiquez avec nous à PublicationsArchive-ArchivesPublications@nrc-cnrc.gc.ca.



A Large Molecular Gas Reservoir in the Protocluster SPT2349–56 at $z = 4.3$

Dazhi Zhou¹, Scott C. Chapman^{1,2,3}, Nikolaus Sulzenauer⁴, Ryley Hill¹, Manuel Aravena⁵, Pablo Araya-Araya⁶, Jared Cathey⁷, Daniel P. Marrone⁸, Kedar A. Phadke^{9,10}, Cassie Reuter¹¹, Manuel Solimano⁵, Justin S. Spilker¹², Joaquin D. Vieira^{9,10,13}, David Vizgan⁹, George C. P. Wang¹, and Axel Weiss⁴

¹ Department of Physics and Astronomy, University of British Columbia, 6225 Agricultural Rd., Vancouver, V6T 1Z1, Canada; dzhou.astro@gmail.com

² Department of Physics and Atmospheric Science, Dalhousie University, Canada

³ National Research Council, Herzberg Astronomy and Astrophysics, Canada

⁴ Max-Planck-Institut für Radioastronomie, Auf dem Hügel 69, 53121 Bonn, Germany

⁵ Instituto de Estudios Astrofísicos, Facultad de Ingeniería y Ciencias, Universidad Diego Portales, Av. Ejército Libertador 441, Santiago, Chile Código Postal 8370191, Chile

⁶ Departamento de Astronomia, Instituto de Astronomia, Geofísica e Ciências Atmosféricas, Universidade de São Paulo, Rua do Matão 1226, Cidade Universitária, 05508-900, São Paulo, SP, Brazil

⁷ Department of Astronomy, University of Florida, Gainesville, FL 32611, USA

⁸ Steward Observatory, University of Arizona, 933 North Cherry Ave., Tucson, AZ 85721, USA

⁹ Department of Astronomy, University of Illinois, 1002 West Green St., Urbana, IL 61801, USA

¹⁰ Center for AstroPhysical Surveys, National Center for Supercomputing Applications, 1205 West Clark St., Urbana, IL 61801, USA

¹¹ Department of Physics, University of California, 366 Physics North MC 7300, Berkeley, CA 94720-7300, USA

¹² Department of Physics and Astronomy and George P. and Cynthia Woods Mitchell Institute for Fundamental Physics and Astronomy, Texas A&M University, 4242 TAMU, College Station, TX 77843-4242, USA

¹³ Department of Physics, University of Illinois, 1110 West Green St., Urbana, IL 61801, USA

Received 2024 December 23; revised 2025 February 7; accepted 2025 February 19; published 2025 March 17

Abstract

We present Atacama Compact Array (ACA) Band-3 observations of the protocluster SPT2349–56, an extreme system hosting >10 ultraluminous infrared galaxies (ULIRGs; $L_{\text{IR}} \gtrsim 10^{12} L_{\odot}$) in a 200 kpc diameter region at $z = 4.3$, to study its integrated molecular gas content via CO(4–3) and the long-wavelength dust continuum. The ~ 30 hr integration represents one of the longest exposures yet taken on a single pointing with the ACA 7 m. The low-resolution ACA data ($21''.0 \times 12''.2$) reveal a 75% excess CO(4–3) flux compared to the sum of individual sources detected in higher-resolution Atacama Large Millimeter/submillimeter Array (ALMA) data ($1''.0 \times 0''.8$). Our work also reveals a similar result by tapering the ALMA data to $10''$. In contrast, the 3.2 mm dust continuum shows little discrepancy between ACA and ALMA. A single-dish [C II] spectrum obtained by APEX/FLASH supports the ACA CO(4–3) result, revealing a large excess in [C II] emission relative to ALMA. The missing flux is unlikely due to undetected faint sources but instead suggests that high-resolution ALMA observations might miss extended and low-surface-brightness gas. Such emission could originate from the circumgalactic medium or the preheated protointracluster medium (proto-ICM). If this molecular gas reservoir replenishes the star formation fuel, the overall depletion timescale will exceed 400 Myr, reducing the requirement for the simultaneous ULIRG activity in SPT2349–56. Our results highlight the role of an extended gas reservoir in sustaining a high star formation rate in SPT2349–56 and potentially establishing the ICM during the transition phase to a mature cluster.

Unified Astronomy Thesaurus concepts: Submillimeter astronomy (1647); Galaxy evolution (594); High-redshift galaxies (734)

1. Introduction

Galaxy clusters are the largest and the densest structures in the local Universe. They are characterized by their high galaxy overdensities but low star formation rates (SFRs), where red and quiescent galaxies are expected to be the main population (e.g., A. Dressler 1980; P. J. E. Peebles 1980; Y.-j. Peng et al. 2010). As the high-redshift progenitors of galaxy clusters, protoclusters reveal the epoch previous to their virialization when their member galaxies were actively forming stars, thereby providing excellent laboratories for studying dark matter halo assembly and the impact of dense environments on galaxy evolution in the early Universe (Y.-K. Chiang et al. 2013, 2017; R. A. Overzier 2016; T. Wang et al. 2016; G. C. Wang et al. 2024). Of particular importance are the

ultraluminous infrared galaxies (ULIRGs; $L_{\text{IR}} \gtrsim 10^{12} L_{\odot}$, $\text{SFR} \gtrsim 100 M_{\odot} \text{ yr}^{-1}$) or submillimeter galaxies (SMGs; $S_{850} \gtrsim 1$ mJy), which represent the most active phase of star formation in massive galaxies. They are important sites of stellar mass buildup in protoclusters and are thought to be the precursors of giant elliptical galaxies in galaxy clusters (e.g., A. W. Blain et al. 2004; P. L. Capak et al. 2011; C. M. Casey et al. 2014; S. Toft et al. 2014; C. M. Casey 2016; J. A. Hodge & E. da Cunha 2020; P. Araya-Araya et al. 2024).

Discovered by the South Pole Telescope (SPT) in the 2500 deg² multiband SPT-Sunyaev–Zel’dovich (SZ) millimeter survey (J. D. Vieira et al. 2010; J. E. Carlstrom et al. 2011; L. M. Mocanu et al. 2013), SPT2349–56 ($z = 4.3$) is the most intensely star-forming protocluster core at $z \sim 4$ confirmed to date (T. B. Miller et al. 2018; G. C. P. Wang et al. 2021). More than 20 protocluster members have been spectroscopically confirmed within a 200 kpc diameter region by submillimeter observations with the Atacama Large Millimeter/submillimeter Array (ALMA), of which at least 11 can be further classified as

ULIRGs on the main sequence within the southern core, meaning that this system contains an extremely high overdensity of ULIRGs compared to other known protoclusters (R. Hill et al. 2020, 2022; K. M. Rotermund et al. 2021; Y. Apostolovski et al. 2024; C. Hughes et al. 2024; A. Venkateshwaran et al. 2024). In the central core region, multiple active galactic nuclei (AGNs) have been detected and the SFR density exceeds $10,000 M_{\odot} \text{ yr}^{-1} \text{ Mpc}^{-3}$ (S. C. Chapman et al. 2024; F. Vito et al. 2024). Simulations suggest that most of the central galaxies will merge to form the brightest cluster galaxy within 1 billion yr (D. Rennehan et al. 2020).

The extreme nature of such protocluster cores continues to challenge our understanding of galaxy formation and evolution (see also Distant Red Core at $z = 4.0$; I. Oteo et al. 2018; R. J. Ivison et al. 2020). To date, no cosmological simulation or galaxy formation model has successfully predicted their ULIRG overdensity (e.g., L. Bassini et al. 2020; D. Rennehan et al. 2020; S. Lim et al. 2021, 2024; K. Fukushima et al. 2023; R.-S. Remus et al. 2023; D. Rennehan 2024; L. Tevlin et al. 2024). Without relying on additional environmental triggers, the ULIRG duty cycle would need to be significantly extended to account for the coeval ULIRG activity observed in such systems (e.g., C. M. Casey 2016). To understand the high SFR density of SPT2349–56, it is crucial to investigate cold molecular gas ($T_{\text{H}_2} \lesssim 100\text{K}$), which serves as the fuel of star formation (R. C. J. Kennicutt 1998). In particular, large and extended cold gas reservoirs are expected in the circumgalactic media (CGM) and intergalactic media in order to sustain the high levels of star formation in protocluster cores (e.g., B. H. C. Emonts et al. 2016, 2018, 2019, 2023b, 2023a; Z. Chen et al. 2024; L. Ghodsi et al. 2024), which is challenging to capture with high-resolution interferometric observations due to their low surface brightness (e.g., C. Cicone et al. 2021; J. Li et al. 2021; G. C. Jones et al. 2023). While ALMA is good at studying the internal properties of individual galaxies, low-resolution data are essential for assessing the global molecular gas reservoir within the system.

In this Letter, we present deep Atacama Compact Array (ACA) observations of CO(4–3) and the 3.2 mm dust continuum to further explore the integrated molecular gas content of the protocluster system SPT2349–56. In Section 2 we describe the ALMA/ACA Band-3 and ancillary APEX/FLASH observations and data reduction. Section 3 presents our estimations of gas mass from three indicators, CO(4–3), the 3.2 mm dust continuum, and [C II], as well as the comparison with previous high-resolution ALMA 12 m results. A discussion and summary are given in Section 4. Throughout the Letter, we follow the Lambda cold dark matter cosmology with $H_0 = 70 \text{ km s}^{-1} \text{ Mpc}^{-1}$ and $\Omega_m = 0.3$, which corresponds to a proper angular scale of $6.88 \text{ kpc}''$ at $z = 4.3$.

2. Observations and Data Reduction

2.1. ALMA Observations

Our ACA Band-3 observations of SPT2349–56 were obtained as part of the Cycle 10 ALMA program (2023.1.00124.S, PI: S. Chapman). We tuned the frequency to place the CO(4–3) line at $z = 4.3$ ($\nu_{\text{obs}} \approx 86.99 \text{ GHz}$) within one of the 1.875 GHz spectral windows in the lower sideband in the “time division modes” (120 channels with 15.625 MHz resolution), covering 85.99–87.86 GHz. The program was carried out between 2024 January and 2024 September, with

41 individual execution blocks (EBs) and a total on-source integration time (t_{int}) of $\sim 30 \text{ hr}$.

We calibrated and reduced the data using the standard calibration script with CASA (version = 6.6.1) in the pipeline mode. Bad measurement sets with short on-source exposures (< 10 minutes) or high phase errors ($> 20^\circ$) were manually discarded after a careful inspection of each initial Quality Assurance (QA0) report, leaving 31 EBs remaining with $t_{\text{int}} \sim 27 \text{ hr}$. Due to the coarse resolution, we performed CLEANING on continuum-subtracted measurement sets using the CASA (version = 6.6.5) task `tclean` with “briggs” (`robust = 0.5`) weighting in the “cube” mode with a “hogbom” deconvolver to produce the data cubes for CO(4–3). The CLEANING process contains two steps. We first cleaned the data to 4σ without a CLEAN mask. We then masked the high-significance 4σ channels with adjacent low-significance 2σ channels (CPROPS mask, E. Rosolowsky & A. Leroy 2006) from the 4σ cleaned data cube and cleaned down to 1σ following the method described in A. K. Leroy et al. (2021). The final product has a synthesized beam of 21.0×12.2 and reaches a line sensitivity of $0.25 \text{ mJy beam}^{-1}$ per channel with a spectral resolution of 54 km s^{-1} .

High-resolution 12 m observations of CO(4–3) with two pointings were observed in C4 configuration for two EBs and in C5 configuration for five EBs, which have $t_{\text{int}} \sim 2.7 \text{ hr}$ for each pointing and reach a maximum recoverable scale (MRS) of 15.1 . [C II] observations were conducted in C3 configuration in three pointings for four EBs ($t_{\text{int}} \sim 0.97 \text{ hr}$, MRS ~ 6.0) and in six pointings in C5 configuration for six EBs ($t_{\text{int}} \sim 0.83 \text{ hr}$, MRS ~ 3.0 ; 2017.1.00273.S, PI: S. Chapman; 2018.1.00058.S, PI: S. Chapman; R. Hill et al. 2020). The corresponding data cubes were obtained in an identical manner as reported in R. Hill et al. (2020), resulting in line sensitivities of $0.07 \text{ mJy beam}^{-1}$ for CO(4–3) and $0.22 \text{ mJy beam}^{-1}$ for [C II], and channel widths of 54 km s^{-1} and 13 km s^{-1} , respectively. The synthesized beams are 1.01×0.84 and 0.35×0.29 , respectively.

Continuum images at 3.2 mm were obtained from line-free channels in “briggs” weighting (`robust = 0.5`) in `mfs` mode with the “hogbom” deconvolver. We used a similar strategy to create the CLEANING mask and cleaned the continuum image down to 1σ . The resulting rms level of the whole image is $22.0 \mu\text{Jy beam}^{-1}$ with beam size of 15.7×10.6 . We produced the 3.2 mm high-resolution Cycle 5 Band-3 continuum map in a similar way, using pixels of 0.15 (2017.1.00273, PI: S. Chapman; R. Hill et al. 2020). The synthesized beam size is 0.94×0.78 and the rms level is $6.0 \mu\text{Jy beam}^{-1}$.

To investigate whether the new ACA results agree with ALMA observations when the resolutions are similar, we produced an ALMA continuum map and CO(4–3) data cube in low resolutions by applying a uv -taper of $10''$, resulting in synthesized beam sizes of 11.0×9.6 , 9.9×9.4 and sensitivities of $0.29 \text{ mJy beam}^{-1}$ per channel, $30.2 \mu\text{Jy beam}^{-1}$ for CO(4–3) and the 3.2 mm dust continuum, respectively.

2.2. APEX Observations

We also used archival single-dish [C II] line observations from the APEX/FLASH receiver as part of Max Planck Society observing time (A. Weiß et al. 2013; B. Gullberg et al. 2015; M. L. Strandet et al. 2016; C. Reuter et al. 2020). The observations were conducted under good weather conditions with an average precipitable water vapor of $\sim 0.3 \text{ mm}$ and a

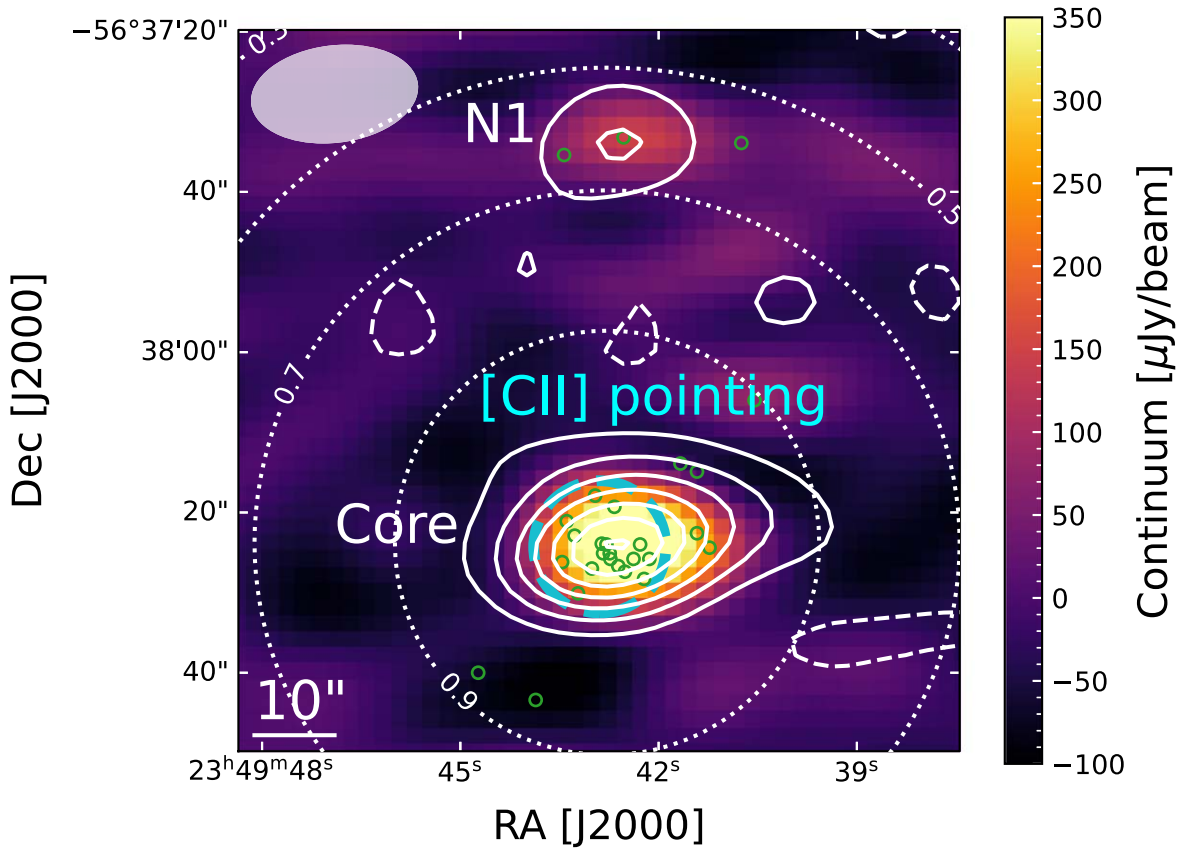


Figure 1. ACA continuum map of the protocluster SPT2349–56 with moment-0 contours of CO(4–3) in the velocity window $[-1373 \text{ km s}^{-1}, 1429 \text{ km s}^{-1}]$ before primary-beam correction. The white solid contours are $[3, 6, 9, 12, 15, 18, 21] \times$ the rms level of the CO emission from ACA observations. The dashed contours are $-2 \times$ the rms level. The white dotted contours indicate $[0.3, 0.5, 0.7, 0.9] \times$ the primary-beam response from the continuum map. The cyan dashed circle represents the main beam of the APEX [C II] observations. Green circles are the locations of all cataloged galaxies from R. Hill et al. (2020). We note that the two sources in the vicinity of “N1” are “NL2” and “N3,” which are not associated with the structure at $z = 4.3$ (R. Hill et al. 2022).

system temperature of $\sim 300 \text{ K}$. The total on-source exposure time is about 2.2 hr. The data were reduced using GILDAS/CLASS. We employed an APEX/FLASH antenna gain¹⁴ of $S_{\nu}/T_A^* = 40 \text{ Jy K}^{-1}$ for the observed frequency $\nu_{\text{obs}} = 358.4 \text{ GHz}$ (B. Gullberg et al. 2015). We subtracted the baseline with a velocity window of 1600 km s^{-1} and the first order polynomial fitting, leading to an rms level of 27 mJy (0.67 mK) for a 100 km s^{-1} channel.

3. Results

3.1. ACA Observations of CO(4–3)

The southern core is only marginally resolved in the ACA observations with the large synthesized beam, allowing a comparison between the integrated CO(4–3) flux and the emission from member galaxies in the protocluster core detected by ALMA (Figure 1). The “N1” source in the northern region is relatively isolated, and so a direct comparison with the high-resolution ALMA result is possible.

First, we used sufficiently large apertures ($30'' \times 17''$) to obtain the overall ACA spectrum. For simplicity, we fit the line with a single Gaussian to determine its width and then integrated over $\pm 3\sigma$ from the mean value ($[-1373 \text{ km s}^{-1}, 1429 \text{ km s}^{-1}]$) to produce an accurate moment-0 map. We varied the size of the elliptical aperture (proportional to the beam shape) and used a curve-of-growth analysis to determine an aperture size that

maximizes the total line strength in the central core. Similarly, we produced a moment-0 map of “N1” with a velocity range of $[-349 \text{ km s}^{-1}, 1429 \text{ km s}^{-1}]$. Since “N1” is unresolved in the ACA map, we used the peak pixel value as the total CO(4–3) line strength.

To calculate the total line strength in the core region recovered by ALMA 12 m observations, we adopted the same source apertures obtained from the curve-of-growth analysis reported in R. Hill et al. (2020) for the spectral extraction of the 22 line emitters in the core region. We then summed these extracted spectra to obtain an overall CO(4–3) spectrum and integrated the flux density over the same velocity range applied to the ACA spectrum.

The spectra of the core region and “N1” from the ACA 7 m and ALMA 12 m observations are shown in Figure 2, revealing an excess line strength from ACA in both cases (Table 1). To ensure the discrepancy is not caused by the potential problem from the absolute flux calibration, we checked their visibilities and corresponding spectra from the tapered ALMA data cube, which also show consistent values (Appendix). We note that ACA 7 m observations have been reported to systematically underestimate line strengths, which on average causes a 27% loss in simulations (e.g., A. K. Leroy et al. 2021, Appendix C). The total CO(4–3) fluxes estimated by ACA observations can only be treated as lower limits.

We then evaluated the CO line luminosity and molecular gas mass (listed in Table 1) with the following formulas

¹⁴ <https://www.apex-telescope.org/telescope/efficiency/>

Table 1

Comparison of Gas Mass Estimates from ACA/APEX Observations to ALMA 12 m Observations in the Three Independent Tracers CO, Dust Continuum, and [C II]

Region	Telescope	$S_{\text{CO}(4-3)\Delta v}$ (Jy km s^{-1})	$L'_{\text{CO}(4-3)}$ ($10^{10} \text{ K km s}^{-1} \text{ pc}^2$)	$M_{\text{H}_2}^{\text{CO}}$ ($10^{10} M_{\odot}$)	$S_{3.2 \text{ mm}}$ (μJy)	$M_{\text{H}_2}^{\text{dust}}$ ($10^{10} M_{\odot}$)	$S_{[\text{C II}]\Delta v}$ (Jy km s^{-1})	$M_{\text{H}_2}^{[\text{C II}]}$ ($10^{10} M_{\odot}$)
(1)	(2)	(3)	(4)	(5)	(6)	(7)	(8)	(9)
Core	ACA/APEX	6.65 ± 0.30	29.3 ± 1.3	185.5 ± 18.2	654 ± 29	84.4 ± 3.7	122.6 ± 11.1	209.4 ± 18.9
	ALMA	3.79 ± 0.12	16.7 ± 0.5	105.7 ± 9.8	754 ± 30	97.2 ± 3.9	52.1 ± 0.2	89.0 ± 0.4
	Excess (%)		75.5 ± 9.6 (CO(4-3))		-13.2 ± 5.1 (dust)		135.3 ± 21.3 ([C II])	
N1	ACA	2.35 ± 0.31	10.4 ± 1.3	65.6 ± 10.3	310 ± 38	39.9 ± 4.9
	ALMA	1.54 ± 0.03	6.77 ± 0.12	42.9 ± 3.8	201 ± 11	25.9 ± 1.4
	Excess (%)		52.8 ± 20.0 (CO(4-3))		54.2 ± 20.7 (dust)	

Note. (1) Regions included in this study. (2) The telescope used for the measurement. (3) Integrated CO(4-3) line strength within $\pm 3\sigma$ of the central velocity. The uncertainty is the primary-beam-corrected rms value of the moment-0 map for the ACA results, and the overall uncertainty through the error propagation from each channel rms for the APEX/ALMA values. (4) CO(4-3) line luminosity in unit of brightness temperature derived from Equation (1). (5) Gas mass estimated from Equation (2). The error includes uncertainties from the measurements and from the chosen α_{CO} and r_{41} values. (6) Total 3.2 mm continuum flux density from Table 2. (7) Gas mass estimated from Equation (3). (8) Integrated [C II] emission line strength within $\pm 800 \text{ km s}^{-1}$ of the central velocity, which is defined by the velocity range for the baseline subtraction. The quoted ALMA values have been corrected for the APEX primary-beam response with a FWHM of $16''.5$. We used the $< -800 \text{ km s}^{-1}$ and $> 800 \text{ km s}^{-1}$ channels to fit the baseline with a first order polynomial for the APEX result. Both errors were obtained from the error propagation. (9) Gas estimates from [C II] line emission with Equation (4).

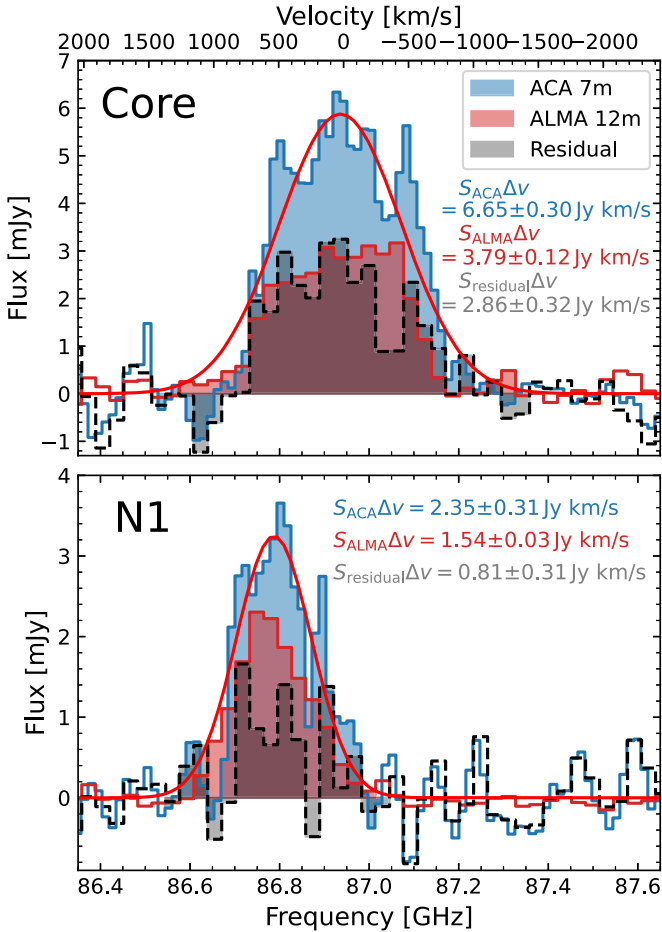


Figure 2. ACA 7 m spectra of CO(4-3) of the southern core and “N1” (blue). The red curves are the best-fit Gaussian profiles for determining the velocity ranges of the moment-0 maps, which are also indicated as the shaded regions. The ALMA 12 m results (obtained by coadding all individually detected galaxies) are shown in red, and the differences between the two measurements are shown in black for comparison. Compared to the ALMA 12 m results, the CO(4-3) line strengths are consistently higher in ACA 7 m observations.

(P. M. Solomon & P. A. Vanden Bout 2005):

$$L'_{\text{CO}(4-3)} = 3.25 \times 10^7 S_{\text{CO}(4-3)\Delta v} \nu_{\text{obs}}^{-2} D_L^2 (1+z)^{-3}, \quad (1)$$

$$M_{\text{H}_2} = \frac{1}{r_{41}} \alpha_{\text{CO}} L'_{\text{CO}(4-3)}, \quad (2)$$

where $L'_{\text{CO}(4-3)}$ is measured in $\text{K km s}^{-1} \text{ pc}^2$, the velocity-integrated line strength $S_{\text{CO}(4-3)\Delta v}$ is in Jy km s^{-1} , the observed frequency ν_{obs} is in GHz, the luminosity distance D_L is in Mpc, and the molecular gas mass M_{H_2} is in M_{\odot} . We adopted a CO(4-3)-to-CO(1-0) line ratio of $r_{41} = 0.60 \pm 0.05$ and a L_{CO} -to- M_{H_2} conversion factor of $\alpha_{\text{CO}} = 3.8 \pm 0.1 M_{\odot}/(\text{K km s}^{-1} \text{ pc}^2)$, which are typical values for high- z SMGs (J. S. Spilker et al. 2014; L. Dunne et al. 2022). However, the integrated gas masses should only be treated as lower limits, as the extended emission could be emitted from potentially more pristine gas and less extreme galaxies, which would result in a substantially higher α_{CO} and lower r_{41} (e.g., A. D. Bolatto et al. 2013; L. J. Tacconi et al. 2013).

3.2. ACA Observations of Dust Continuum

To investigate whether the low-resolution observations result in systematically higher values across different tracers, we further compared the long-wavelength dust continuum (often used as a tracer of gas mass, e.g., N. Scoville et al. 2016, 2017, 2023; L. Dunne et al. 2022) in the core region and in “N1” using the same ACA and 12 m data. As the 3.2 mm continua have not been significantly detected in most proto-cluster members, we summed the flux densities of sources with a 4σ detection and scaled the undetected sources from their $850 \mu\text{m}$ flux densities to avoid the large uncertainty. We tested three separate methods: we recorded the continua measured from the peak pixel values, we integrated the surface brightness within Kron apertures ($k=2.5$, $R_{\text{min}}=3.5$) using SourceExtractor (version 2.28.0, E. Bertin & S. Arnouts 1996), and we modeled the image using a single-component 2D Gaussian using the CASA task `imfit` (Table 2). Considering the complex

Table 2
3.2 mm Source Catalog from the ACA and ALMA Observations

ID	R.A.	Decl.	Distance	S/N	PB	S_{peak}	S_{Kron}	S_{fit}	S_{best}	Counterpart
(1)	(deg)	(deg)	(arcsec)	(5)	(6)	(μJy)	(μJy)	(μJy)	(μJy)	(11)
	(2)	(3)	(4)			(7)	(8)	(9)	(10)	
1 ^a	357.4278	-56.6387	4.6	18.3	1.00	110 ± 6	149 ± 12	142 ± 12	149 ± 12	C1(A)
2	357.4225	-56.6396	9.5	12.9	0.92	85 ± 7	95 ± 13	98 ± 8	98 ± 8	C4(D)
3 ^a	357.4284	-56.6403	2.6	13.9	0.99	84 ± 6	106 ± 10	119 ± 15	106 ± 10	C6, C13, C16(CG)
4 ^a	357.4282	-56.6400	1.9	19.6	0.99	119 ± 6	137 ± 12	155 ± 17	137 ± 12	C3, C12(B)
5 ^a	357.4218	-56.6402	10.8	6.7	0.89	45 ± 7	87 ± 16	70 ± 16	87 ± 16	C8(E)
6	357.4256	-56.6405	3.8	9.5	0.97	59 ± 6	65 ± 14	61 ± 8	59 ± 6	C5(F)
7	357.4259	-56.6411	4.9	4.4	0.95	28 ± 6	31 ± 15	28 ± 7	28 ± 6	C9(I)
rest ^b	$S_{850,\text{total}} = 4.67 \pm 0.32 \text{ mJy}$					$f_{\text{cor}} = 52.0 \pm 4.5$			90 ± 10	...
Core (12 m)	754 ± 30	...
Core ^a (ACA)	357.4272	-56.6399	...	22.6	1.00	499 ± 22	654 ± 29	712 ± 28	654 ± 29	...
N1 ^a (12 m)	357.4272	-56.6259	2.0	24.1	1.00	169 ± 7	201 ± 11	180 ± 10	201 ± 11	...
N1 (ACA)	357.4262	-56.6261	...	8.1	0.57	310 ± 38	223 ± 35	238 ± 52	310 ± 38	...

Notes. See Section 3.2 for details. (1) Source ID. (2)–(3) Source coordinate of the peak in the continuum map. (4) The distance from the peak position of the ALMA sources to the peak position of the ACA source. (5) The signal-to-noise ratio (S/N) of the peak flux density obtained in the continuum map before primary-beam correction. (6) The primary-beam response of the ACA/ALMA map. (7) The peak flux density and corresponding rms level after the primary-beam correction. (8) The total flux within a Kron aperture determined by `SourceExtractor` with the primary-beam correction. The uncertainty is obtained from the standard deviation of 10,000 random Kron apertures placed on the continuum map before primary-beam correction and then corrected by the beam response. (9) The primary-beam-corrected flux density estimated with a single-component 2D Gaussian fit using `imfit` in CASA. (10) Our best estimate of the continuum flux density after visual inspections. We adopted the peak value for the unresolved sources, the model flux density for the resolved sources that can be well fit by a 2D Gaussian profile, and the aperture flux density for the resolved sources with a complex morphology. (11) The corresponding counterpart identified from R. Hill et al. (2020) and T. B. Miller et al. (2018).

^a The source is resolved and displays a complex morphology. We chose the aperture flux as the best result.

^b Because a substantial number of sources remain undetected, we calculated the average $S_{850 \mu\text{m}}/S_{3.2 \text{ mm}}$ ratio f_{cor} from the seven detected sources and estimated the overall scaled 3.2 mm flux from the undetected sources.

extended structure of the integrated core galaxies versus the compact continuum source in “N1,” we adopted the Kron aperture flux and the peak value for the 3.2 mm continuum in the core region and “N1,” respectively.

We ran `SourceExtractor` again in a similar manner to estimate the 3 mm continuum recovered by the ALMA 12 m data. We recorded the three independent measurements for sources with significant detections ($>4\sigma$). We carefully inspected the Kron apertures and image cuts of each source and determined their flux densities based on their compactness and morphologies. We note that only seven sources (corresponding to 10 of the cataloged galaxies due to blending) that lie within the ACA 2σ continuum contour of the core region have been detected by the 12 m data, leaving 12 confirmed protocluster members remaining undetected due to the faintness of their long-wavelength continua. To account for the continuum fluxes from these undetected sources, we estimated their expected 3 mm continuum levels based on their 850 μm flux densities with the scaling factor $S_{850 \mu\text{m}}/S_{3.2 \text{ mm}}$ obtained from the detected sources.

As shown in Table 2, the “N1” source has a somewhat ($\approx 50\%/2.6\sigma$) higher 3.2 mm continuum with ACA than we measured with the 12 m data, which could be caused by the contribution from faint surrounding galaxies (e.g., interlopers “NL2” and “N3”) or the large uncertainty of “N1,” which is away from the phase center of the ACA pointing. This is supported by the fact that “N1” only shows a mild increase in continuum flux when the ALMA continuum map is tapered (Appendix), which suggests that its dust continuum could be overestimated from the ACA continuum map. In contrast, compared to the sum of the 12 m source measurements, the core region shows a comparable or even weaker 3.2 mm

continuum ($\approx -10\%/-2.6\sigma$) with ACA. However, the differences from ACA to 12 m in both the core and “N1” are still within 3σ uncertainties.

We note that the lower continuum level in the core region measured with the ACA may be a result of a smaller contribution from noise boosting for the unresolved core, or contamination from the SZ effect in the low-resolution data (R. A. Sunyaev & Ya. B. Zeldovich 1970; D. Zhou et al. 2024 and 2025, in preparation). However, the contrast with the large excess in CO(4–3) found by ACA suggests the difference between CO(4–3) and the continuum is most likely astrophysical in origin, which will be discussed in Section 4.

We used the following formula to estimate the gas mass from the 3.2 mm dust continuum in units of $10^{10} M_{\odot}$ (N. Scoville et al. 2016, 2017, 2023):

$$M_{\text{H}_2} = 1.78 S_{\text{obs}} (1+z)^{-(\beta+3)} \left(\frac{\nu_{850}}{\nu_{\text{obs}}} \right)^{\beta+2} D_{\text{L}}^2, \quad (3)$$

where S_{obs} is the observed continuum flux density in the unit of mJy, β is the dust emissivity index, ν_{850} and ν_{obs} are the frequencies at 850 μm and at the observed wavelength, and the luminosity distance D_{L} is in Gpc. We used the typical emissivity index of $\beta = 2$ for the calculation. The estimated continuum-derived gas masses are also shown in Table 1 for comparison.

3.3. APEX Observations of [C II]

Considering the discrepancies seen in ACA versus 12 m through two gas tracers, CO(4–3) and the long-wavelength dust continuum, we also utilized archival APEX observations to see

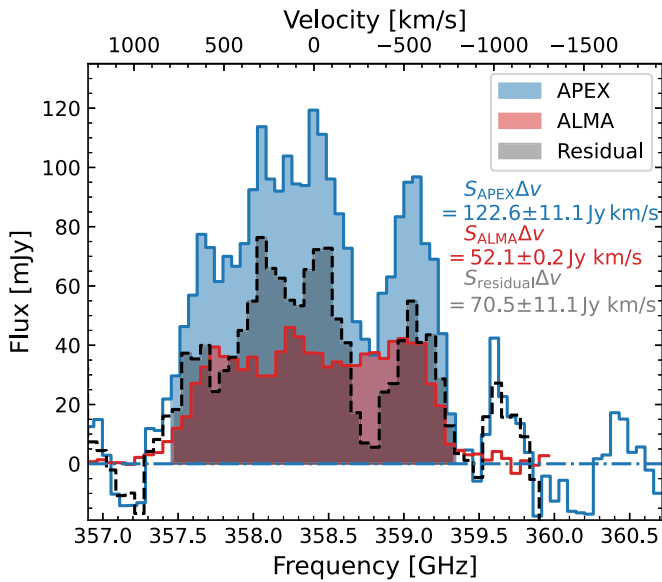


Figure 3. [C II] spectrum from APEX/FLASH observations (blue) compared to the scaled and coadded ALMA spectra of all individually detected protocluster members within the APEX beam (red). The difference is shown in black. For the purpose of this plot, we slightly smoothed the APEX spectrum with a low-pass Savitzky–Golay filter with a polynomial order of 1 to suppress the high-frequency noise. Since we use $\pm 800 \text{ km s}^{-1}$ for the baseline subtraction, only the excluded channels (shaded) were used for calculating the integrated line strength. The excess in [C II] line strength from the APEX observations supports our ACA result.

if an excess exists in [C II], also an indicator of gas mass (e.g., C. L. Carilli & F. Walter 2013; A. Zanella et al. 2018). Figure 3 shows the [C II] spectrum of the protocluster core, where the pointing center and beam are indicated on Figure 1. To compare the APEX spectrum to the integrated [C II] emission from individual sources detected with ALMA, the APEX beam response must be taken into account. We first obtained the spectra of the individual ALMA [C II] sources in a manner identical to that described in Section 3.1. We then calculated their distance to the APEX beam center and corrected the corresponding 12 m [C II] spectra for the APEX beam response. For simplicity, we used a Gaussian function to approximate the APEX beam for each ALMA source attenuation and treated the galaxies as point sources. The integrated [C II] line strength was obtained within a range of $\pm 800 \text{ km s}^{-1}$ from the line center, which is defined by the boundary of the baseline subtraction of the APEX spectrum.

We note that the pointing on APEX introduces some uncertainties into the beam center. Considering ≈ 200 dumps are included in ~ 20 hr of observations (including calibrations), some effective beam size uncertainty may be introduced. We thus considered a range of beam sizes from 16.5 to $20''$ for the correction. Compared to the standard FWHM of 16.5 , the largest beam size ($20''$) results in a 9% difference of the integrated ALMA [C II] flux, which is small compared to the calibration uncertainty. Therefore, we adopted the observatory-suggested beam size of 16.5 for our comparison (Table 1).

We then calculated the [C II] luminosity and the gas mass from the following relations (P. M. Solomon & P. A. Vanden Bout 2005; A. Zanella et al. 2018):

$$L_{[\text{C II}]} = 1.04 \times 10^{-3} S_{[\text{C II}]} \Delta v \nu_{\text{rest}} (1+z)^{-1} D_L^2, \quad (4)$$

$$M_{\text{H}_2} = \alpha_{[\text{C II}]} L_{[\text{C II}]}, \quad (5)$$

where the [C II] line luminosity $L_{[\text{C II}]}$ is in units of L_{\odot} , the velocity-integrated line strength $S_{[\text{C II}]} \Delta v$ is in Jy km s^{-1} , the luminosity distance D_L is in Mpc, and the gas mass M_{H_2} is in M_{\odot} . For the derived gas mass in Table 1 we used the standard [C II]-to- H_2 conversion factor $\alpha_{[\text{C II}]} = 30 M_{\odot}/L_{\odot}$ (e.g., A. Zanella et al. 2018; R. Decarli et al. 2022). We note that due to the APEX beam response, the measured [C II] flux is underestimated, which is only used for comparison purposes.

4. Discussion and Summary

In Section 3 we compared the emissions from three different gas tracers, CO(4–3), dust continuum at 3.2 mm, and [C II], measured from high-resolution ALMA 12 m observations and low-resolution ACA 7 m and APEX/FLASH observations. We found that compared to the dust continuum, both CO(4–3) and [C II] show a significant excess in the low-resolution data. As the flux loss from the aperture measurement is only up to about 10% (R. Hill et al. 2020), the finite aperture size is less likely to miss such a large amount of the emission. We also carefully investigated CO(4–3) in the uv -tapered ALMA data cube and the uv -plane and concluded that the discrepancies were not caused by the absolute calibration uncertainties (Appendix), suggesting a significant fraction of emission should not arise from the interstellar medium (ISM) of the confirmed protocluster members.

It is of interest to understand the possible origins of the additional gas captured by the low-resolution data. First, some faint line emitters might be missed due to the limited sensitivity. R. Hill et al. (2020) adopted a strict threshold for [C II]-emitter selection (signal-to-noise ratio (S/N) ≥ 6.2) to ensure a high fidelity. A missing population of faint emitters might contribute a considerable amount of [C II] and CO(4–3) emission (N. Sulzner et al. 2025, in preparation). However, additional >100 faint line emitters with $F_{\text{CO}(4-3)} \gtrsim 0.03 \text{ Jy km s}^{-1}$ would be required to account for the missing CO(4–3) emission in the central 100 kpc radius region. Such a number of faint emitters cannot be accommodated by the current luminosity function in SPT2349–56, where the flat faint end is reasonably well constrained (R. Hill et al. 2020).

Alternatively, the discrepancy could be due to the extended CGM around protocluster galaxies (e.g., B. H. C. Emonts et al. 2016, 2023a; Z. Chen et al. 2024; M. Solimano et al. 2024). Literature studies of CO(1–0) in high- z galaxies indicate ubiquitous extended CO(1–0) halos, which suggests that a bulk of molecular gas (up to 80%) arises from clumpy dense clouds outside of star-forming regions (e.g., R. J. Ivison et al. 2011; M. Frias Castillo et al. 2023; Z. Chen et al. 2024; M. Rybak et al. 2024). It is possible that the molecular CGM arises from outflows caused by stellar or AGN feedback (e.g., A. Weiß et al. 2001; F. Walter et al. 2002; D. Lutz et al. 2020; R. C. Levy et al. 2021; I. Montoya Arroyave et al. 2024), which was trapped by the deep potential well of SPT2349–56 and accelerates the baryon cycle process (e.g., M. Ginolfi et al. 2020; C.-A. Faucher-Giguère & S. P. Oh 2023; T. A. Thompson & T. M. Heckman 2024).

The “negative CLEANing bowls” in high-resolution interferometric data is a common artifact caused by inadequate uv sampling when the extended emission is overresolved, which appear as negative regions spatially and spectrally around bright emission lines in deconvolved data cubes. This feature has been identified from the [C II] spectra of protocluster

members in the ALMA 12 m observations (see R. Hill et al. 2020, Appendix A), suggesting missing extended components in the current high-resolution data cube (e.g., I. Czekala et al. 2021; A. K. Leroy et al. 2021; N. Sulzenauer et al. 2025, in preparation). A significant flux loss is expected due to the inadequate CLEANing, which is usually pronounced in more diffuse emission and the higher-resolution data. It naturally explains the discrepancies from the three different gas tracers. An accurate CLEAN mask with a perfect CLEANing is needed to recover the flux loss.

Another possible origin of the missing flux could be the very extended gas reservoir, permeating the protocluster core before virialized heating occurs (i.e., the “protointracluster medium” or proto-ICM, e.g., C. Dong et al. 2023; K. E. Heintz et al. 2024), which would have low surface brightness and may reach the MRS ($\sim 15''$) of previous ALMA configurations. Some preprocessing processes such as ram pressure stripping, tidal interaction, and harassment are expected in such a crowded field, causing a substantial amount of gas to be stripped but remain in the protocluster (e.g., S. Alberts & A. Noble 2022; L. Tevlin et al. 2024). Interestingly, despite the discrepancy in derived gas mass seen between the different tracers (Table 1), the gas masses derived from CO(4–3) and from the dust continuum show a good agreement in the ALMA 12 m data, which indicates that the CO(4–3) and dust continuum emission captured by the high-resolution interferometric observations trace the same gas component. The consistent dust continuum but higher CO(4–3) emission in the ACA observations imply a very high gas-to-dust ratio of this extra gas, which is difficult to reach by the ISM but plausible from a preheated intracluster medium (e.g., M. Giard et al. 2008).

Indeed, the deeper [C II] observations not only discover additional faint [C II] emitters, but also reveal extended “[C II] streamers,” suggesting that a fraction of cold gas is not in the form of the ISM or the CGM (R. Hill et al. 2020; N. Sulzenauer et al. 2025, in preparation). But the “[C II] streamers” only contribute to $\sim 5\%$ of the total [C II] emission in current ALMA data, which cannot fully explain the excess flux (N. Sulzenauer et al. 2025, in preparation). In addition, the consistently high [C I](2–1)/[C I](1–0) ratios of the protocluster members in SPT2349–56 also point to a scenario where cold gas might have been stripped and remains in the form of the CGM or proto-ICM (C. Hughes et al. 2024). In this case, the missing flux can be recovered with a heavy *uv*-tapering when its corresponding *uv*-distance is larger than the shortest baseline. For emission that arises from even a larger scale, the compact configurations of ALMA and the additional observations with the ACA 7 m and even the total-power (TP) array might be needed to add more short spacings to recover the large-scale missing flux.

The end point of this additional extended gas is unclear. It could be a reservoir replenishing the star formation fuel, or the early stage of the emergent proto-ICM before heating during virialization. If the gas can be efficiently accreted onto the protocluster galaxies, it could provide a sustained fuel, counteracting the rapid gas depletion caused by high SFRs. By adopting the total SFR estimated by R. Hill et al. (2020) and our updated gas mass for the core region, we reevaluated the gas-depletion timescale. The overall depletion time becomes $\gtrsim 400$ Myr, which significantly relaxes the synchronization requirements for >10 coeval ULIRGs in SPT2349–56 (C. M. Casey 2016). If there is no further accretion from the

cosmic web, the high SFRs can still be maintained until $z \sim 3$, when the quenching is expected to take place. Beyond its potential role in fueling star formation, this gas could also represent the cold phase of the emergent ICM. During this transition phase, the cold gas could begin to accumulate and interact within the protocluster environment, eventually heating itself through gravitational relaxation while evolving into a mature galaxy cluster (R.-S. Remus et al. 2023).

In summary, we have presented deep ACA Band-3 observations of CO(4–3) and the 3.2 mm dust continuum in the protocluster SPT2349–56. Compared to the high-resolution ALMA 12 m observations, the ACA observations show a 75% excess in CO(4–3), but a smaller difference in the 3.2 mm continuum flux. We also utilized archival APEX observations to show that [C II] emission is also 135% higher in the single-dish data compared to the ALMA 12 m data.

Our analysis shows that the discrepancies in the flux excess from these gas tracers are not likely to be caused by missing faint galaxies, since the faint end of the luminosity function would need to be far steeper than previously constrained. Instead, the origin of the missing flux could arise from the extended emission, either from the large-scale CGM or the more diffused cold “proto-ICM” before virialized heating. The observed excess gas suggests the buildup of the nascent ICM, or an extended gas reservoir that can prolong the depletion time and enable the high SFRs simultaneously observed across >10 ULIRGs in SPT2349–56. Strategies such as deep CLEANing, *uv*-tapering, or adding more short spacings from the ALMA compact configurations or the ACA and TP arrays might help recover the missing flux in high-resolution ALMA observations of systems similar to SPT2349–56.

Acknowledgments

We thank John E. Carlstrom, Kevin Harrington, Daizhong Liu, Padelis Papadopoulos, and Douglas Rennehan for useful discussions on this work. This research used the Canadian Advanced Network For Astronomy Research (CANFAR) operated in partnership by the Canadian Astronomy Data Centre and The Digital Research Alliance of Canada with support from the National Research Council of Canada, the Canadian Space Agency, CANARIE, and the Canadian Foundation for Innovation. This Letter makes use of the following ALMA data: ADS/JAO.ALMA#2017.1.00273.S, ADS/JAO.ALMA#2018.1.00058.S, and ADS/JAO.ALMA#2023.1.00124.S. ALMA is a partnership of ESO (representing its member states), NSF (USA) and NINS (Japan), together with NRC (Canada), MOST and ASIAA (Taiwan), and KASI (Republic of Korea), in cooperation with the Republic of Chile. The Joint ALMA Observatory is operated by ESO, AUI/NRAO, and NAOJ. The National Radio Astronomy Observatory is a facility of the National Science Foundation operated under cooperative agreement by Associated Universities, Inc. This publication is based on data acquired with the Atacama Pathfinder Experiment (APEX). APEX is a collaboration between the Max-Planck-Institut für Radioastronomie, the European Southern Observatory, and the Onsala Space Observatory. The SPT is supported by the National Science Foundation through grant PLR-1248097, with partial support through PHY-1125897, the Kavli Foundation, and the Gordon and Betty Moore Foundation grant GBMF 947. D.Z., S.C.C., R.H., and G.C.P.W. acknowledge support from NSERC-6740. M.A. acknowledges support from ANID Basal Project FB210003 and ANID MILENIO NCN2024_112. M.S. was financially supported by

Becas-ANID scholarship #21221511 and also acknowledges support from ANID BASAL project FB210003.

Facilities: ALMA (S. Claude et al. 2008), APEX (S. Heyminck et al. 2006).

Software: astropy (Astropy Collaboration et al. 2022), spectral_cube (A. Ginsburg et al. 2019), GILDAS/CLASS (J. Pety 2005), numpy (C. R. Harris et al. 2020), scipy (P. Virtanen et al. 2020), matplotlib (J. D. Hunter 2007), CASA (CASA Team et al. 2022), uvplot (M. Tazzari 2019), SourceExtractor (E. Bertin & S. Arnouts 1996).

Appendix Visibility Analysis

To compare if the difference seen in ACA observations is caused by the absolute calibration uncertainties, we also measured the integrated CO(4–3) flux and 3.2 mm continuum flux density of the southern core directly in the visibility plane, which avoids potential issues from the overresolved flux with the CLEANing. The uv -coverage of ACA and ALMA data is shown in Figure 4 (left panel).

For the CO(4–3) emission, we used the continuum-subtracted measurement sets obtained from CASA task `uvcontsub` and spectrally averaged them over the velocity range within $1.2 \times \text{FWHM}$ of the line width with CASA task `split` and compensated the flux loss measured in the ACA spectrum to maximize the S/N (M. Novak et al. 2020). We then scaled the visibilities by the corresponding velocity range

and calculated weight-average visibility in each uv -distance bin. For the comparison of the continuum flux densities, we flagged all channels associated with CO emission and averaged all channels in each spectral window to obtain visibilities of the dust continuum. The $\sim 2''$ offset in the phase centers of two observations was corrected with the `uvplot` function `apply_phase`. Because an accurate multicomponent fitting is beyond the scope of this work, we only compared the vector-averaged amplitudes of the visibilities of ACA and ALMA observations obtained from `uvplot`. As shown in Figure 5, the visibility amplitudes of both CO(4–3) and the 3.2 mm continuum are consistent at a similar uv -distance, which suggests that the discrepancy should not be caused by the flux scale from different amplitude calibrations.

We note that the uv -distance of the MRS ($d_{uv} \sim 13.75 \text{ k}\lambda$) of the ALMA observations is longer than its shortest baseline. To investigate if the extra diffuse emission can still be captured by ALMA, we tapered the ALMA data to a lower resolution by $10''$ (Figure 4, right) and obtained the spectra of the southern core and “N1” (Figure 6). We measured their corresponding integrated CO(4–3) fluxes and continuum flux densities in an identical manner as in Section 3.1 (Table 3). Despite a larger uncertainty, the values of the CO(4–3) fluxes and 3.2 mm dust continuum flux densities are consistent with the ACA results. We concluded that the extended gas reservoir can still be recovered by current available ALMA data, which requires an aggressive uv -tapering.

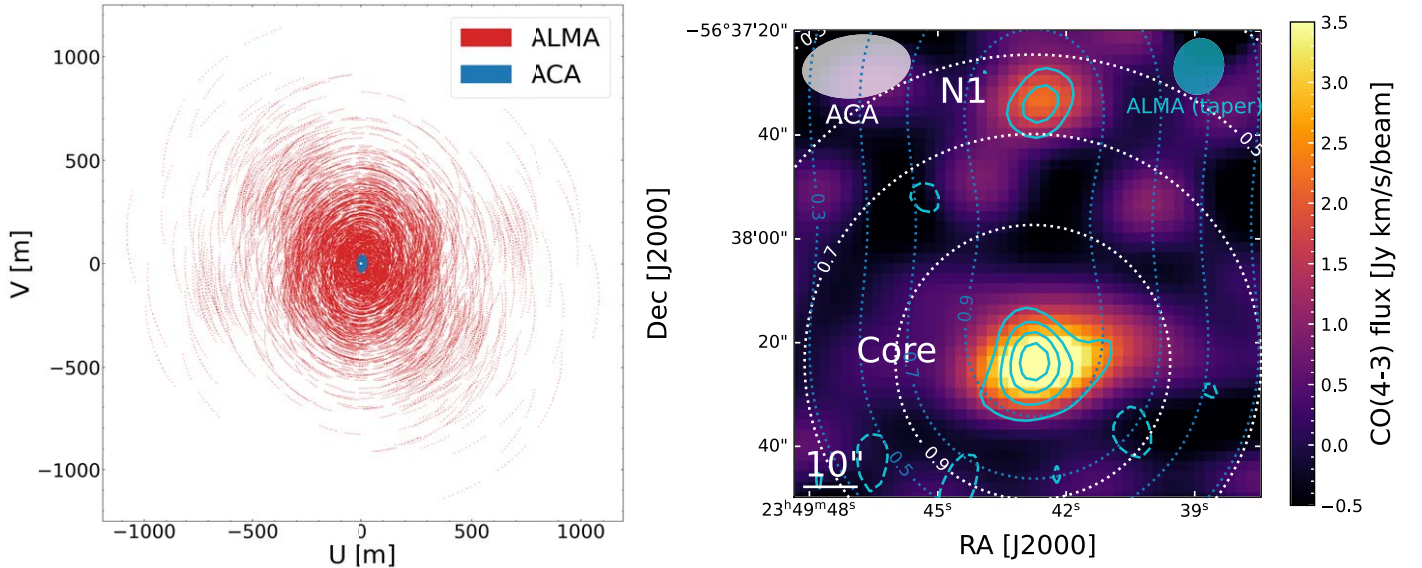


Figure 4. Left: uv -coverage of ACA (blue) and ALMA (red) observations. Right: ACA CO(4–3) moment-0 map overlaid with tapered ALMA CO(4–3) moment-0 contours. Details and line styles are similar to Figure 1. The synthesized beams of ACA (white) and tapered ALMA (blue) are shown in the top left and top right.

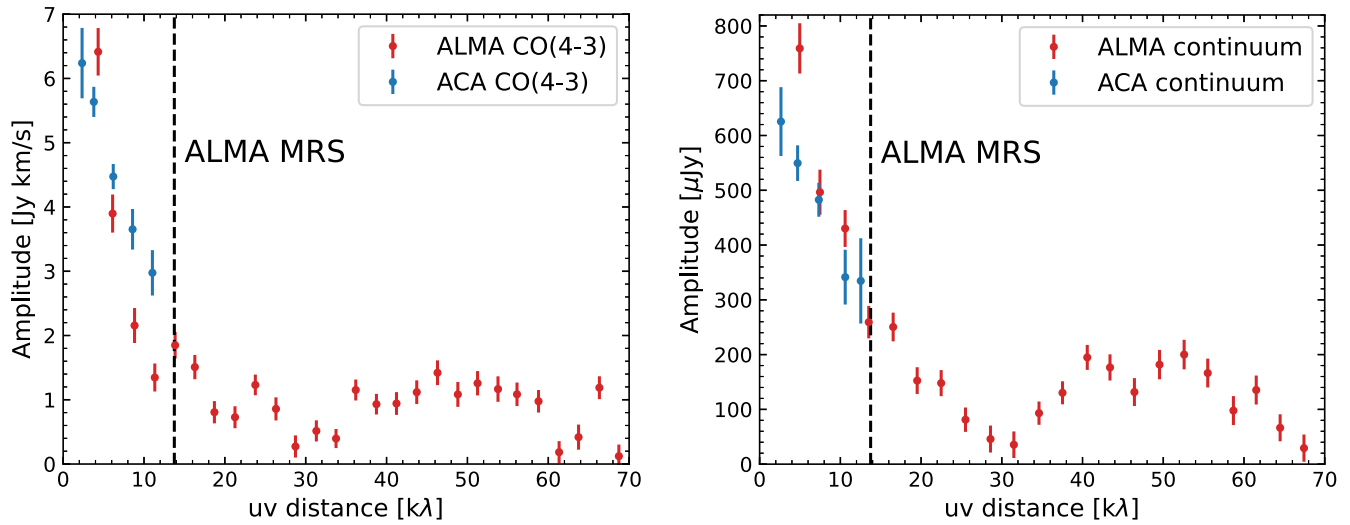


Figure 5. Amplitudes of CO(4–3) and 3.2 mm dust continuum of the southern core from the ALMA (red) and ACA (blue) observations in the visibility plane. The MRS of the ALMA 12 m observations is shown as black dashed lines. Visibilities show a good agreement at similar uv distance, which suggests that CO(4–3) excess in ACA observations is not caused by the absolute calibration uncertainty.

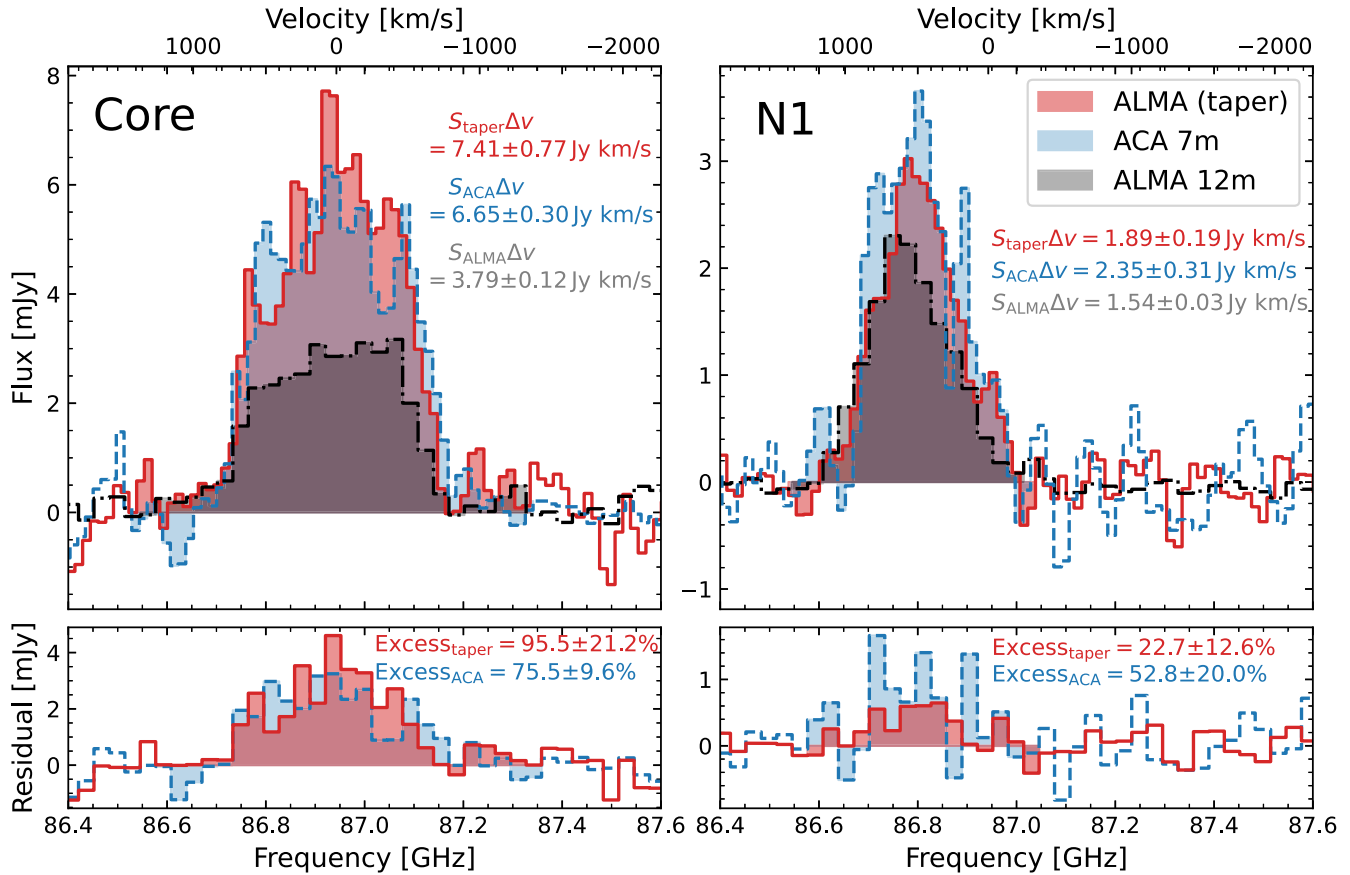


Figure 6. CO(4–3) spectra of core and “N1” from the tapered ALMA (red) compared to untapered ALMA (gray) and ACA (blue) data (top panels). The extra fluxes from the low-resolution results are plotted in the bottom panels. CO(4–3) excess is also shown in tapered ALMA data cube.

Table 3








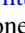








CO(4–3) Fluxes and 3.2 mm Flux Densities of the Southern Core and “N1” Source Measured from High-resolution ALMA, Tapered ALMA, and ACA Data

Image	$S_{\text{CO(4-3),core}} \Delta v$ (Jy km s ⁻¹)	$S_{3.2 \text{ mm,core}}^a$ (μJy)	$S_{\text{CO(4-3),N1}} \Delta v$ (Jy km s ⁻¹)	$S_{3.2 \text{ mm,N1}}^a$ (μJy)
(1)	(2)	(3)	(4)	(5)
ALMA	3.79 ± 0.12	754 ± 30	1.54 ± 0.03	201 ± 11
ALMA (tapered)	7.41 ± 0.77	667 ± 48	1.89 ± 0.19	211 ± 55
Tapered excess (%)	95.5 ± 21.2	-11.5 ± 7.1	22.7 ± 12.6	4.8 ± 28.0
ACA	6.65 ± 0.30	654 ± 29	2.35 ± 0.31	310 ± 38
ACA excess (%)	75.5 ± 9.6	-13.2 ± 5.1	52.8 ± 20.0	54.2 ± 20.7

Notes. (1) Image used for the measurements. (2) Integrated CO(4–3) line strength of the southern core within $\pm 3\sigma$ of the central velocity. The reported uncertainty is the primary-beam-corrected rms value. (3) 3.2 mm continuum flux density of the southern core within a Kron aperture obtained by `SourceExtractor`. The uncertainty is obtained from the primary-beam-corrected standard deviation of values from 1000 random Kron apertures. (4) Integrated CO(4–3) line strength of “N1.” (5) 3.2 mm continuum flux density of “N1” within a Kron aperture.

^a The source displays a complex morphology. We chose the aperture flux as the result.

ORCID iDs

Dazhi Zhou  <https://orcid.org/0000-0002-6922-469X>
 Scott C. Chapman  <https://orcid.org/0000-0002-8487-3153>
 Nikolaus Sulzenauer  <https://orcid.org/0000-0002-3187-1648>
 Ryley Hill  <https://orcid.org/0009-0008-8718-0644>
 Manuel Aravena  <https://orcid.org/0000-0002-6290-3198>
 Pablo Araya-Araya  <https://orcid.org/0000-0003-2860-5717>
 Jared Cathey  <https://orcid.org/0000-0002-4657-7679>
 Daniel P. Marrone  <https://orcid.org/0000-0002-2367-1080>
 Kedar A. Phadke  <https://orcid.org/0000-0001-7946-557X>
 Cassie Reuter  <https://orcid.org/0000-0001-7477-1586>
 Manuel Solimano  <https://orcid.org/0000-0001-6629-0379>
 Justin S. Spilker  <https://orcid.org/0000-0003-3256-5615>
 Joaquin D. Vieira  <https://orcid.org/0000-0001-7192-3871>
 David Vizgan  <https://orcid.org/0000-0001-7610-5544>
 George C. P. Wang  <https://orcid.org/0009-0003-4626-9777>
 Axel Weiss  <https://orcid.org/0000-0003-4678-3939>

References

- Alberts, S., & Noble, A. 2022, *Univ*, 8, 554
 Apostolovski, Y., Aravena, M., Anguita, T., et al. 2024, *A&A*, 683, A64
 Araya-Araya, P., Cochrane, R. K., Hayward, C. C., et al. 2024, *ApJ*, 977, 204
 Astropy Collaboration, Price-Whelan, A. M., Lim, P. L., et al. 2022, *ApJ*, 935, 167
 Bassini, L., Rasia, E., Borgani, S., et al. 2020, *A&A*, 642, A37
 Bertin, E., & Arnouts, S. 1996, *A&AS*, 117, 393
 Blain, A. W., Chapman, S. C., Smail, I., & Ivison, R. 2004, *ApJ*, 611, 725
 Bolatto, A. D., Wolfire, M., & Leroy, A. K. 2013, *ARA&A*, 51, 207
 Capak, P. L., Riechers, D., Scoville, N. Z., et al. 2011, *Natur*, 470, 233
 Carilli, C. L., & Walter, F. 2013, *ARA&A*, 51, 105
 Carlstrom, J. E., Ade, P. A. R., Aird, K. A., et al. 2011, *PASP*, 123, 568
 CASA Team, Bean, B., Bhatnagar, S., et al. 2022, *PASP*, 134, 114501
 Casey, C. M. 2016, *ApJ*, 824, 36
 Casey, C. M., Narayanan, D., & Cooray, A. 2014, *PhR*, 541, 45
 Chapman, S. C., Hill, R., Aravena, M., et al. 2024, *ApJ*, 961, 120
 Chen, Z., Dannerbauer, H., Lehnert, M. D., et al. 2024, *MNRAS*, 527, 8950
 Chiang, Y.-K., Overzier, R., & Gebhardt, K. 2013, *ApJ*, 779, 127
 Chiang, Y.-K., Overzier, R. A., Gebhardt, K., & Henriques, B. 2017, *ApJL*, 844, L23
 Cicone, C., Mainieri, V., Circo, C., et al. 2021, *A&A*, 654, L8
 Claude, S., Jiang, F., Niranjanan, P., et al. 2008, *Proc. SPIE*, 7020, 70201B
 Czekala, I., Loomis, R. A., Teague, R., et al. 2021, *ApJS*, 257, 2
 Decarli, R., Pensabene, A., Venemans, B., et al. 2022, *A&A*, 662, A60
 Dong, C., Lee, K.-G., Ata, M., Horowitz, B., & Momose, R. 2023, *ApJL*, 945, L28
 Dressler, A. 1980, *ApJ*, 236, 351
 Dunne, L., Maddox, S. J., Papadopoulos, P. P., Ivison, R. J., & Gomez, H. L. 2022, *MNRAS*, 517, 962
 Emonts, B. H. C., Cai, Z., Prochaska, J. X., Li, Q., & Lehnert, M. D. 2019, *ApJ*, 887, 86
 Emonts, B. H. C., Lehnert, M. D., Dannerbauer, H., et al. 2018, *MNRAS*, 477, L60
 Emonts, B. H. C., Lehnert, M. D., Lebowitz, S., et al. 2023a, *ApJ*, 952, 148
 Emonts, B. H. C., Lehnert, M. D., Villar-Martín, M., et al. 2016, *Sci*, 354, 1128
 Emonts, B. H. C., Lehnert, M. D., Yoon, I., et al. 2023b, *Sci*, 379, 1323
 Faucher-Giguère, C.-A., & Oh, S. P. 2023, *ARA&A*, 61, 131
 Frias Castillo, M., Hodge, J., Rybak, M., et al. 2023, *ApJ*, 945, 128
 Fukushima, K., Nagamine, K., & Shimizu, I. 2023, *MNRAS*, 525, 3760
 Ghodsi, L., Zhou, J., Andreani, P., et al. 2024, *A&A*, 689, A67
 Giard, M., Montier, L., Pointecouteau, E., & Simmat, E. 2008, *A&A*, 490, 547
 Ginolfi, M., Jones, G. C., Béthermin, M., et al. 2020, *A&A*, 633, A90
 Ginsburg, A., Koch, E., Robitaille, T., et al. 2019, radio-astro-tools/spectral-cube: v0.4.4, Zenodo, doi:10.5281/zenodo.2573901
 Gullberg, B., De Breuck, C., Vieira, J. D., et al. 2015, *MNRAS*, 449, 2883
 Harris, C. R., Millman, K. J., van der Walt, S. J., et al. 2020, *Natur*, 585, 357
 Heintz, K. E., Bennett, J. S., Oesch, P. A., et al. 2024, arXiv:2407.06287
 Heyminck, S., Kasemann, C., Güsten, R., de Lange, G., & Graf, U. U. 2006, *A&A*, 454, L21
 Hill, R., Chapman, S., Phadke, K. A., et al. 2022, *MNRAS*, 512, 4352
 Hill, R., Chapman, S., Scott, D., et al. 2020, *MNRAS*, 495, 3124
 Hodge, J. A., & da Cunha, E. 2020, *RSOS*, 7, 200556
 Hughes, C., Hill, R., Chapman, S., et al. 2024, arXiv:2412.03790
 Hunter, J. D. 2007, *CSE*, 9, 90
 Ivison, R. J., Biggs, A. D., Bremer, M., Arumugam, V., & Dunne, L. 2020, *MNRAS*, 496, 4358
 Ivison, R. J., Papadopoulos, P. P., Smail, I., et al. 2011, *MNRAS*, 412, 1913
 Jones, G. C., Maiolino, R., Carniani, S., et al. 2023, *MNRAS*, 522, 275
 Kennicutt, R. C. J. 1998, *ApJ*, 498, 541
 Leroy, A. K., Hughes, A., Liu, D., et al. 2021, *ApJS*, 255, 19
 Levy, R. C., Bolatto, A. D., Leroy, A. K., et al. 2021, *ApJ*, 912, 4
 Li, J., Emonts, B. H. C., Cai, Z., et al. 2021, *ApJL*, 922, L29
 Lim, S., Scott, D., Babul, A., et al. 2021, *MNRAS*, 501, 1803
 Lim, S., Tacchella, S., Schaye, J., et al. 2024, *MNRAS*, 532, 4551
 Lutz, D., Sturm, E., Janssen, A., et al. 2020, *A&A*, 633, A134
 Miller, T. B., Chapman, S. C., Aravena, M., et al. 2018, *Natur*, 556, 469
 Mocanu, L. M., Crawford, T. M., Vieira, J. D., et al. 2013, *ApJ*, 779, 61
 Montoya Arroyave, I., Cicone, C., Andreani, P., et al. 2024, *A&A*, 686, A47
 Novak, M., Venemans, B. P., Walter, F., et al. 2020, *ApJ*, 904, 131
 Oteo, I., Ivison, R. J., Dunne, L., et al. 2018, *ApJ*, 856, 72
 Overzier, R. A. 2016, *A&ARv*, 24, 14
 Peebles, P. J. E. 1980, *The Large-scale Structure of the Universe* (Princeton, NJ: Princeton Univ. Press)
 Peng, Y.-j., Lilly, S. J., Kovač, K., et al. 2010, *ApJ*, 721, 193
 Pety, J. 2005, in SF2A-2005: Semaine de l’Astrophysique Française, ed. F. Casoli et al. (Strasbourg: EdP-Sciences), 721
 Remus, R.-S., Dolag, K., & Dannerbauer, H. 2023, *ApJ*, 950, 191
 Rennehan, D. 2024, *ApJ*, 975, 114
 Rennehan, D., Babul, A., Hayward, C. C., et al. 2020, *MNRAS*, 493, 4607
 Reuter, C., Vieira, J. D., Spilker, J. S., et al. 2020, *ApJ*, 902, 78
 Rosolowsky, E., & Leroy, A. 2006, *PASP*, 118, 590
 Rotermund, K. M., Chapman, S. C., Phadke, K. A., et al. 2021, *MNRAS*, 502, 1797
 Rybak, M., Jansen, J. T., Frias Castillo, M., et al. 2024, arXiv:2411.06474
 Scoville, N., Faisst, A., Weaver, J., et al. 2023, *ApJ*, 943, 82

- Scoville, N., Lee, N., Vanden Bout, P., et al. 2017, [ApJ](#), **837**, 150
- Scoville, N., Sheth, K., Aussel, H., et al. 2016, [ApJ](#), **820**, 83
- Solimano, M., González-López, J., Aravena, M., et al. 2024, [A&A](#), **689**, A145
- Solomon, P. M., & Vanden Bout, P. A. 2005, [ARA&A](#), **43**, 677
- Spilker, J. S., Marrone, D. P., Aguirre, J. E., et al. 2014, [ApJ](#), **785**, 149
- Strandet, M. L., Weiss, A., Vieira, J. D., et al. 2016, [ApJ](#), **822**, 80
- Sunyaev, R. A., & Zeldovich, Ya. B. 1970, [Ap&SS](#), **7**, 3
- Tacconi, L. J., Neri, R., Genzel, R., et al. 2013, [ApJ](#), **768**, 74
- Tazzari, M. 2019, uvplot: Interferometric Visibilities Plotter, Astrophysics Source Code Library, ascl:[1911.002](#)
- Tevlin, L., Berlok, T., Pfrommer, C., et al. 2024, arXiv:[2411.00103](#)
- Thompson, T. A., & Heckman, T. M. 2024, [ARA&A](#), **62**, 529
- Toft, S., Smolčić, V., Magnelli, B., et al. 2014, [ApJ](#), **782**, 68
- Venkateshwaran, A., Weiss, A., Sulzenauer, N., et al. 2024, [ApJ](#), **977**, 161
- Vieira, J. D., Crawford, T. M., Switzer, E. R., et al. 2010, [ApJ](#), **719**, 763
- Virtanen, P., Gommers, R., Oliphant, T. E., et al. 2020, [NatMe](#), **17**, 261
- Vito, F., Brandt, W. N., Comastri, A., et al. 2024, [A&A](#), **689**, A130
- Walter, F., Weiss, A., & Scoville, N. 2002, [ApJL](#), **580**, L21
- Wang, G. C., Chapman, S. C., Sulzenauer, N., et al. 2024, arXiv:[2406.16637](#)
- Wang, G. C. P., Hill, R., Chapman, S. C., et al. 2021, [MNRAS](#), **508**, 3754
- Wang, T., Elbaz, D., Daddi, E., et al. 2016, [ApJ](#), **828**, 56
- Weiß, A., De Breuck, C., Marrone, D. P., et al. 2013, [ApJ](#), **767**, 88
- Weiß, A., Neininger, N., Hüttemeister, S., & Klein, U. 2001, [A&A](#), **365**, 571
- Zanella, A., Daddi, E., Magdis, G., et al. 2018, [MNRAS](#), **481**, 1976
- Zhou, D., Greve, T. R., Gullberg, B., et al. 2024, [A&A](#), **690**, A196